One-loop formulas for $H \to Z\nu_l\bar{\nu}_l$ for $l = e, \mu, \tau$ in 't Hooft-Veltman gauge

Dzung Tri Tran, Khiem Hong Phan

Institute of Fundamental and Applied Sciences, Duy Tan University, Ho Chi Minh City 700000*, Vietnam*
Faculty of Natural Sciences, Duy Tan University, Da Nang City 550000*, Vietnam*

arXiv:2211.15116v2 [hep-ph] 7 Mar 2023

Abstract

In this paper, we present analytical results for one-loop contributing to the decay processes $H \to Z\nu_l\bar{\nu}_l$ (for $l = e, \mu, \tau$). The calculations are performed within the Standard Model framework in 't Hooft-Veltman gauge. One-loop form factors are then written in terms of scalar one-loop functions in the standard notations of `LoopTools`. As a result, one-loop decay rates for the decay channels can be evaluated numerically by using the package. Furthermore, we analyse the signals of $H \to Z\nu_l\bar{\nu}_l$ via the production processes $e^-e^+ \to ZH^* \to Z(H^* \to Z\nu_l\bar{\nu}_l)$ including the initial beam polarizations at future lepton collider. The Standard Model backgrounds such as the processes $e^-e^+ \to \nu_l\bar{\nu}_l ZZ$ are also examined in this study. In numerical results, we find that one-loop corrections are about 10% contributions to the decay rates. They are sizeable contributions and should be taken into account at future colliders. We show that the signals $H \to Z\nu_l\bar{\nu}_l$ are clearly visible at center-of-mass energy $\sqrt{s} = 250$ GeV and are hard to probe at higher-energy regions due to the dominant of the backgrounds.

Keywords: Higgs phenomenology, One-loop Feynman integrals, Analytic methods for Quantum Field Theory, Dimensional regularization, Future colliders.

1. Introduction

After discovering Standard-Model-like (SM-like) Higgs boson at the Large Hadron Collider (LHC) [1, 2], the high-precision measurements for the properties of the SM-like Higgs boson are the most important tasks at the High-Luminosity LHC (HL-LHC) [3, 4] and future lepton colliders [5]. In other words, all Higgs productions and its decay channels should be probed as precisely as possible at future colliders. From these data, we can verify the SM at higher-energy regions as well as extract the new physics. Among the Higgs decay channels, $H \to Z\nu_l\bar{\nu}_l$ for $l = e, \mu, \tau$ are of interests for several aspects. First, one considers $Z \to \nu_l\bar{\nu}_l$ in final state, the decay processes are corresponding to $H \to$ invisible particles which have recently studied at the LHC [6]. Search for invisible Higgs-boson decays play a key role for explaining the existence of dark matter. Furthermore, the decay channels also contribute to $H \to$ lepton pair plus missing energy when $Z \to$ lepton pair is concerned in final state. These contributions are also useful to evaluate precisely the SM backgrounds for the decay rates of $H \to$ lepton pair in final state. As above reasons, the precise decay rates for $H \to Z\nu_l\bar{\nu}_l$ could provide an important tool for testing SM at higher-energy scales and for probing new physics.

One-loop contributing to $H \to Z\nu_l\bar{\nu}_l$ have computed in [7] and for $H \to 4$ fermions have presented in [8, 9, 10]. In this paper, we evaluate the one-loop contributions for the decay processes $H \to Z\nu_l\bar{\nu}_l$ for $l = e, \mu, \tau$ in 't Hooft-Veltman gauge. In comparison with the previous calculations, we perform this computation with the following advantages. First, we focus on the

Email address: `phanhongkhiem@duytan.edu.vn` (Khiem Hong Phan)

analytical calculations for the decay channels and show a clear analytical structure for the one-loop amplitude of $H \to Z\nu_l\bar{\nu}_l$ in this paper. As a result, we can explain and extract the dominant contributions to the decay widths when these are necessary (the dominant contributions are from Z-pole diagrams, or the diagrams of $H \to ZZ^* \to Z\nu_l\bar{\nu}_l$ in the decay channels as we show in later sections). Furthermore, off-shell Higgs decays are also valid in our work. In addition, one can generalize the couplings of Nambu-Goldstone bosons with Higgs, gauge bosons, etc (as our previous work in [11]). We are easily to extend our results to many of beyond the Standard models. Since Nambu-Goldstone bosons play the same role like the changed Higgs in the extensions of the Standard Model Higgs sector. Last but not least, the signals of $H \to Z\nu_l\bar{\nu}_l$ via Higgs productions at future lepton colliders are studied in our works. In further detail, one-loop form factors are expressed in terms of scalar one-loop Passarino-Veltman functions (called as PV-functions hereafter) in the standard notations of `LoopTools`. As a result, one can evaluate the decay rates numerically by using the package. Moreover, the signals of $H \to Z\nu_l\bar{\nu}_l$ through Higgs productions at future lepton collider, for instance, the processes $e^-e^+ \to ZH^* \to Z(Z\nu_l\bar{\nu}_l)$ with including initial beam polarizations are generated. The Standard Model backgrounds such as $e^-e^+ \to \nu_l\bar{\nu}_l ZZ$ are also included in this analyse. In phenomenological results, we find that one-loop corrections are about 10% contributions to the decay rates. They are sizeable contributions and should be taken into account at future colliders. We show that the signals $H \to Z\nu_l\bar{\nu}_l$ are clearly visible at center-of-mass energy $\sqrt{s} = 250$ GeV and these are hard to probe at higher-energy regions due to the dominant of the backgrounds.

The layout of the paper is as follows: In section 2, we present the calculations for $H \to Z\nu_l\bar{\nu}_l$ in detail. We then show phenomenological results for the computations. Decay rates for on-shell and off-shell Higgs decay modes are studied with including the unpolarized and longitudinally polarized Z boson in the final states. The signals of $H \to Z\nu_l\bar{\nu}_l$ via the Higgs productions at future lepton colliders are also generated in this section. Conclusions for this work are discussed in the section 4. In the appendies, we first summary all tensor reduction formulas for one-loop integrals appear in this work. Numerical checks for the calculations are presented. All self-energy and counter-terms for the decay processes are shown in detail. One-loop Feynman diagrams in 't Hooft-Veltman gauge for this decay channels are shown in the appendix E.

2. Calculations

We are going to present the calculations for $H(p_H) \to Z(q_1)\nu_l(q_2)\bar{\nu}_l(q_3)$ in detail. For these computations, we are working in t 'Hooft-Veltman gauge. Within the SM framework, all Feynman diagrams can be grouped in several classifications showing in the Appendix E. In group G_0, we have tree Feynman diagram contributing to the decay processes. For group G_1, we include all one-loop Feynman diagrams correcting to the vertex $Z\nu_l\bar{\nu}_l$. We then list all Z-pole Feynman diagrams in group G_2 and non Z-pole diagrams in group G_3. The counterterm diagrams for this decay channels are classified into group G_4.

In general, the amplitude for $H(p_H) \to Z(q_1)\nu_l(q_2)\bar{\nu}_l(q_3)$ can be decomposed by the following Lorentz structure:

$$\mathcal{A}_{H\to Z\nu_l\bar{\nu}_l} = \Big\{F_{00}g^{\mu\nu} + F_{12}\, q_1^\nu q_2^\mu + F_{13}\, q_1^\nu q_3^\mu\Big\}\Big[\bar{u}(q_2)\gamma_\nu P_L v(q_3)\Big]\varepsilon_\mu^*(q_1). \tag{1}$$

Where F_{00}, F_{12} and F_{13} are form factors including both tree-level and one-loop diagram contributions. The form factors are functions of the Mandelstam invariants such as $s_{ij} = (q_i + q_j)^2$ for $i \neq j = 1, 2, 3$ and mass-squared in one-loop diagrams. One also verifies that $s_{12} + s_{13} + s_{23} = M_H^2 + M_Z^2$. In Eq. (1), projection operator $P_L = (1 - \gamma_5)/2$ is taken into account and the term $\varepsilon_\mu^*(q_1)$ is polarization vector of final Z boson. Our computations can be summarized as

follows. We first write down Feynman amplitude for all diagrams mentioned above. By using `Package-X` [12], all Dirac traces and Lorentz contractions in d dimensions are performed. The amplitudes are then casted into tensor one-loop integrals. The tensor integrals are next reduced to scalar PV-functions [13]. It is noted that all the relevant tensor reduction formulas are shown in appendix A. The PV-functions can be evaluated numerically by using `LoopTools`.

All form factors are calculated from Feynman diagrams in 't Hooft-Veltman gauge and their expressions are presented in this section. For tree-level diagram, the form factor is given by:

$$F_{00}^{(G_0)}(s_{12},s_{13},s_{23}) = \frac{2\pi\alpha}{s_W^2 c_W^3}\frac{M_W}{s_{23}-M_Z^2+i\Gamma_Z M_Z}. \tag{2}$$

Where $s_W(c_W)$ is sine (cosine) of Weinberg angle, respectively and Γ_Z is decay width of Z boson.

At one-loop level, all form factors are taken the form of

$$F_{ij} = \sum_{G=\{G_1,\cdots,G_4\}} F_{ij}^{(G)}(s_{12},s_{13},s_{23}), \quad \text{for } ij=\{00,12,13\}. \tag{3}$$

Where $\{G_1,\cdots,G_4\} = \{\text{group } 1,\cdots,\text{group } 4\}$ are corresponding to the groups of Feynman diagrams in the appendix E. By considering each group of Feynman diagram, analytic results for all form factors are presented in the following paragraphs. Taking the attribution from group G_1, we have one-loop form factors accordingly

$$\begin{aligned} F_{00}^{(G_1)}(s_{12},s_{13},s_{23}) &= -\frac{\alpha^2}{8s_W^4 c_W^5}\frac{M_W}{s_{23}-M_Z^2+i\Gamma_Z M_Z}\times \\ &\times\Big\{ -8c_W^4 B_0(s_{23},M_W^2,M_W^2) - 2\Big[c_W^2(4s_W^2-2)+1\Big]B_0(s_{23},0,0) \\ &-8c_W^4\Big[2C_{00}-s_{23}(C_1+C_2)\Big](0,s_{23},0,0,M_W^2,M_W^2) \\ &-4c_W^2(2s_W^2-1)\Big[M_W^2 C_0+s_{23}C_2-2C_{00}\Big](s_{23},0,0,0,0,M_W^2) \\ &+\Big[4C_{00}-2s_{23}C_2-2M_Z^2C_0\Big](s_{23},0,0,0,0,M_Z^2)+(2c_W^2+1)\Big\}, \end{aligned} \tag{4}$$

$$F_{ij}^{(G_1)}(s_{12},s_{13},s_{23}) = 0, \quad \text{for} \quad ij=\{12,13\}. \tag{5}$$

For group G_2 of Feynman diagram, the form factors can be divided into the fermion and boson parts as follows:

$$F_{00}^{(G_2)}(s_{12},s_{13},s_{23}) = \frac{\alpha^2}{24\, s_W^4 c_W^7 M_W}\frac{1}{(s_{23}-M_Z^2+i\Gamma_Z M_Z)^2}\Big[\sum_f N_f^C F_{00,f}^{(G_2)} + F_{00,b}^{(G_2)}\Big]. \tag{6}$$

Where N_f^C is color number. It takes 3 for quarks and 1 for leptons. For the fermion contributions,

we take top quark loop as example, analytic results are written as

$$
\begin{aligned}
F_{00,f}^{(G_2)} &= 2c_W^2 M_W^2\Big[8s_W^2(4s_W^2-3)+9\Big]\times \\
&\qquad\times\Big[A_0(m_t^2)+s_{23}B_1(s_{23},m_t^2,m_t^2)-2B_{00}(s_{23},m_t^2,m_t^2)\Big] \\
&+2m_t^2c_W^2\Big\{9M_W^2-2c_W^2(M_Z^2-s_{23})\Big[4s_W^2(4s_W^2-3)+9\Big]\Big\}B_0(s_{23},m_t^2,m_t^2) \\
&+m_t^2c_W^4(s_{23}-M_Z^2)\Big\{36m_t^2+\Big[8s_W^2(4s_W^2-3)+9\Big](s_{12}+s_{13})\Big\}\times \\
&\qquad\times C_0(M_Z^2,s_{23},M_H^2,m_t^2,m_t^2,m_t^2) \\
&-m_t^2c_W^4(M_Z^2-s_{23})\Big\{(M_H^2+5M_Z^2-s_{23})\Big[8s_W^2(4s_W^2-3)+9\Big] \\
&\qquad+8s_W^2(3-4s_W^2)(s_{12}+s_{13})\Big\}C_1(M_Z^2,s_{23},M_H^2,m_t^2,m_t^2,m_t^2) \\
&-2m_t^2c_W^4(M_Z^2-s_{23})\Big\{9M_H^2+\Big[8s_W^2(4s_W^2-3)+9\Big](s_{12}+s_{13})\Big\}\times \\
&\qquad\times C_2(M_Z^2,s_{23},M_H^2,m_t^2,m_t^2,m_t^2) \\
&+8m_t^2c_W^4(M_Z^2-s_{23})\Big[8s_W^2(4s_W^2-3)+9\Big]C_{00}(M_Z^2,s_{23},M_H^2,m_t^2,m_t^2,m_t^2).
\end{aligned}
\tag{7}
$$

The contribution from boson part reads

$$
\begin{aligned}
F_{00,b}^{(G_2)} &= 8c_W^6 M_W^2 s_{23} - 6M_W^2 c_W^2\Big[3c_W^2(4c_W^2-1)+s_W^2\Big]A_0(M_W^2) - 3M_W^2 c_W^2\Big[A_0(M_Z^2)+A_0(M_H^2)\Big] \\
&+\frac{3}{2}c_W^4 M_H^2(M_Z^2-s_{23})B_0(M_H^2,M_Z^2,M_Z^2) + 12M_W^2 s_W^4 c_W^4(M_Z^2-s_{23})B_0(M_Z^2,M_W^2,M_W^2) \\
&+3c_W^4(M_Z^2-s_{23})\Big[c_W^4(M_H^2+24M_W^2) - 2M_H^2 s_W^2 c_W^2 + M_H^2 s_W^4\Big]B_0(M_H^2,M_W^2,M_W^2) \\
&+12M_W^2 c_W^2\Big\{(2M_W^2+5s_{23})c_W^4 - 2M_W^2 s_W^4 \\
&\qquad +(M_Z^2-s_{23})\Big[s_W^4 - 2c_W^2(c_W^2+1)\Big]c_W^2\Big\}B_0(s_{23},M_W^2,M_W^2) \\
&+6M_W^2 c_W^2(M_Z^2-s_{23})\Big[B_0(M_Z^2,M_H^2,M_Z^2)+B_0(s_{23},M_H^2,M_Z^2)\Big] - 12M_W^4 B_0(s_{23},M_H^2,M_Z^2) \\
&-4M_W^2 c_W^2\Big[40s_W^2(4s_W^2-3)+63\Big]B_{00}(s_{23},0,0) + 12M_W^2 c_W^2 B_{00}(s_{23},M_H^2,M_Z^2) \\
&+12M_W^2 c_W^2\Big(9c_W^4 - 2s_W^2 c_W^2 + s_W^4\Big)B_{00}(s_{23},M_W^2,M_W^2) \\
&+\frac{9}{2}c_W^4 M_H^2(M_Z^2-s_{23})B_0(M_H^2,M_H^2,M_H^2) \\
&+2M_W^2 c_W^2 s_{23}\Big[40s_W^2(4s_W^2-3)+63\Big]B_1(s_{23},0,0) + 24c_W^6 M_W^2 s_{23}B_1(s_{23},M_W^2,M_W^2) \\
&-12M_W^2 c_W^6(M_Z^2-s_{23})[4M_Z^2+c_W^2(s_{12}+s_{13})]C_1(M_Z^2,s_{23},M_H^2,M_W^2,M_W^2,M_W^2) \\
&+24M_W^2 c_W^6(M_Z^2-s_{23})(-c_W^2 M_H^2 - s_{12}-s_{13})C_2(M_Z^2,s_{23},M_H^2,M_W^2,M_W^2,M_W^2) \\
&-12M_W^2 c_W^4(M_Z^2-s_{23})\Big\{2c_W^4\Big[2M_W^2+5M_Z^2-2(s_{12}+s_{13})\Big] - (M_H^2+2M_W^2)s_W^4 \\
&\qquad +s_W^2 c_W^2\Big(M_H^2+2M_W^2+s_{12}+s_{13}\Big)\Big\}C_0(M_Z^2,s_{23},M_H^2,M_W^2,M_W^2,M_W^2) \\
&-12c_W^4(M_Z^2-s_{23})\Big[s_W^2(s_W^2-2c_W^2)(M_H^2+2M_W^2) \\
&\qquad +(M_H^2+18M_W^2)c_W^4\Big]C_{00}(M_Z^2,s_{23},M_H^2,M_W^2,M_W^2,M_W^2) \\
&+18M_H^2 c_W^2(s_{23}-M_Z^2)\Big[-M_W^2 C_0 + c_W^2 C_{00}\Big](M_H^2,s_{23},M_Z^2,M_H^2,M_H^2,M_Z^2) \\
&+(M_Z^2-s_{23})\Big[12M_W^4 C_0 - 6c_W^2(M_H^2 c_W^2+2M_W^2)C_{00}\Big](M_Z^2,M_H^2,s_{23},M_H^2,M_Z^2,M_Z^2).
\end{aligned}
\tag{8}
$$

Other one-loop form factors are given the same convention as

$$
\begin{aligned}
F_{12}^{(G_2)}(s_{12},s_{13},s_{23}) &= F_{13}^{(G_2)}(s_{13},s_{12},s_{23}) \\
&= -\frac{\alpha^2}{12s_W^4 c_W^5 M_W}\frac{1}{s_{23}-M_Z^2+i\Gamma_Z M_Z}\Big[\sum_f N_f^C F_{12,f}^{(G_2)} + F_{12,b}^{(G_2)}\Big].
\end{aligned}
\tag{9}
$$

Each part in the above equation reads the form of (we also take top quark loop as an example for fermion contributions)

$$
\begin{aligned}
F_{12,f}^{(G_2)} &= 9m_t^2 c_W^2 C_1(M_Z^2,s_{23},M_H^2,m_t^2,m_t^2,m_t^2) \\
&+m_t^2 c_W^2\Big[8s_W^2(4s_W^2-3)+9\Big]\Big[C_0+4\Big(C_2+C_{12}+C_{22}\Big)\Big](M_Z^2,s_{23},M_H^2,m_t^2,m_t^2,m_t^2)
\end{aligned}
\tag{10}
$$

and

$$
\begin{aligned}
F_{12,b}^{(G_2)} &= -12c_W^2M_W^2\Big[\big(5c_W^4-2c_W^2s_W^2+s_W^4\big)C_0+C_1\Big](M_Z^2,s_{23},M_H^2,M_W^2,M_W^2,M_W^2) \\
&\quad +3c_W^2M_H^2\Big[C_{12}(M_Z^2,M_H^2,s_{23},M_H^2,M_Z^2,M_Z^2) \\
&\qquad\qquad -3\Big(C_1+C_{11}+C_{12}\Big)(M_H^2,s_{23},M_Z^2,M_H^2,M_H^2,M_Z^2)\Big] \\
&\quad +6M_W^2\Big[C_1+C_2+C_{12}\Big](M_Z^2,M_H^2,s_{23},M_H^2,M_Z^2,M_Z^2) \\
&\quad -6c_W^2\Big[s_W^2(s_W^2-2c_W^2)(M_H^2+2M_W^2)+c_W^4(M_H^2+18M_W^2)\Big] \\
&\qquad\qquad \times\Big[C_2+C_{12}+C_{22}\Big](M_Z^2,s_{23},M_H^2,M_W^2,M_W^2,M_W^2).
\end{aligned}
\tag{11}
$$

We change to the contributions of all Feynman diagrams in group G_3. For this group, there is no Z-pole diagrams including in one-loop form factors. But we have one-loop box diagrams. There are triple gauge boson vertex and the propagator of lepton, or two propagators of leptons in one-loop box diagrams, we hence have tensor box integrals which the highest rank is up to $R = 2$ in the amplitude. It is explained that the corresponding form factors are expressed in

terms of the PV-functions C- and up to D_{33}-coefficients.

$$
\begin{aligned}
F_{00}^{(G_3)} &= \frac{\alpha^2 M_W}{4 s_W^4 c_W^5} \times \qquad (12)\\
&\times \Bigg\{ 2c_W^4 \Big[(2s_W^2-1) C_0(M_Z^2,0,s_{13},0,0,M_W^2) + (3c_W^2+1) C_0(0,s_{23},0,0,M_W^2,M_W^2) \\
&\qquad + C_2(0,M_H^2,s_{13},0,M_W^2,M_W^2) + C_2(0,M_H^2,s_{12},0,M_W^2,M_W^2) \Big] \\
&+ C_0(M_Z^2,0,s_{13},0,0,M_Z^2) + C_2(0,M_H^2,s_{13},0,M_Z^2,M_Z^2) + C_2(0,M_H^2,s_{12},0,M_Z^2,M_Z^2) \\
&+ 8c_W^6 \Big[D_{00}(s_{12},M_Z^2,s_{23},0,0,M_H^2,0,M_W^2,M_W^2,M_W^2) \\
&\qquad + D_{00}(s_{13},M_Z^2,s_{23},0,0,M_H^2,0,M_W^2,M_W^2,M_W^2) \Big] \\
&- 2c_W^6 \Big[(2M_Z^2+s_{12}) D_1(s_{12},M_Z^2,s_{23},0,0,M_H^2,0,M_W^2,M_W^2,M_W^2) \\
&\qquad + (2M_Z^2+s_{13}) D_1(s_{13},M_Z^2,s_{23},0,0,M_H^2,0,M_W^2,M_W^2,M_W^2) \Big] \\
&+ c_W^4 \Big\{ \Big[2c_W^2(3M_H^2-2s_{23}-3s_{13}) + s_W^2(s_{13}-M_H^2) \Big] \times \\
&\qquad \times D_3(s_{13},M_Z^2,s_{23},0,0,M_H^2,0,M_W^2,M_W^2,M_W^2) \\
&\quad + \Big[s_W^2(s_{12}-M_H^2) + 2c_W^2(3M_H^2-2s_{23}-3s_{12}) \Big] \times \\
&\qquad \times D_3(s_{12},M_Z^2,s_{23},0,0,M_H^2,0,M_W^2,M_W^2,M_W^2) \Big\} \\
&+ c_W^4 (3c_W^2+1) \Big[(M_W^2-s_{12}) D_0(s_{12},M_Z^2,s_{23},0,0,M_H^2,0,M_W^2,M_W^2,M_W^2) \\
&\qquad + (M_W^2-s_{13}) D_0(s_{13},M_Z^2,s_{23},0,0,M_H^2,0,M_W^2,M_W^2,M_W^2) \Big] \\
&+ (s_{12}-M_Z^2) \Big[2c_W^4(1-2s_W^2) D_2(M_Z^2,s_{12},M_H^2,s_{13},0,0,0,0,M_W^2,M_W^2) \\
&\qquad - D_2(M_Z^2,s_{12},M_H^2,s_{13},0,0,0,0,M_Z^2,M_Z^2) \Big] \\
&+ s_W^2 c_W^4 \Big[(M_Z^2-s_{13}) D_2(s_{13},M_Z^2,s_{23},0,0,M_H^2,0,M_W^2,M_W^2,M_W^2) \\
&\qquad + (M_Z^2-s_{12}) D_2(s_{12},M_Z^2,s_{23},0,0,M_H^2,0,M_W^2,M_W^2,M_W^2) \Big] \\
&+ (s_{23}+s_{12}) \Big[2c_W^4(2s_W^2-1) D_3(M_Z^2,s_{12},M_H^2,s_{13},0,0,0,0,M_W^2,M_W^2) \\
&\qquad + D_3(M_Z^2,s_{12},M_H^2,s_{13},0,0,0,0,M_Z^2,M_Z^2) \Big] \\
&+ \Big[M_Z^2 D_0 + s_{12} D_1 - 2D_{00} \Big] (M_Z^2,s_{12},M_H^2,s_{13},0,0,0,0,M_Z^2,M_Z^2) \\
&+ 2c_W^4(1-2s_W^2) \Big[2D_{00} - s_{12} D_1 - M_W^2 D_0 \Big] (M_Z^2,s_{12},M_H^2,s_{13},0,0,0,0,M_W^2,M_W^2) \Bigg\}.
\end{aligned}
$$

In addition, we have other form factors which are expressed as follows:

$$
\begin{aligned}
F_{12}^{(G_3)} &= \frac{\alpha^2 M_W}{2 s_W^4 c_W^5}\Bigg\{ \Big[D_2 + D_{12} + D_{23}\Big](M_Z^2, s_{12}, M_H^2, s_{13}, 0, 0, 0, 0, M_Z^2, M_Z^2) \\
&\quad -4c_W^6\Big[D_3 + D_{13}\Big](s_{13}, M_Z^2, s_{23}, 0, 0, M_H^2, 0, M_W^2, M_W^2, M_W^2) \\
&\quad -2c_W^4(1-2s_W^2)\Big[D_2 + D_{12} + D_{23}\Big](M_Z^2, s_{12}, M_H^2, s_{13}, 0, 0, 0, 0, M_W^2, M_W^2) \\
&\quad +2c_W^4\Big[2c_W^2\Big(D_{11} + D_{12}\Big) + (s_W^2 - c_W^2)D_2\Big](s_{12}, M_Z^2, s_{23}, 0, 0, M_H^2, 0, M_W^2, M_W^2, M_W^2)\Bigg\}, \qquad (13) \\
F_{13}^{(G_3)} &= \frac{\alpha^2 M_W}{2 s_W^4 c_W^5}\Bigg\{ -\Big[D_{13} + D_{33}\Big](M_Z^2, s_{12}, M_H^2, s_{13}, 0, 0, 0, 0, M_Z^2, M_Z^2) \\
&\quad -4c_W^6\Big[D_3 + D_{13}\Big](s_{12}, M_Z^2, s_{23}, 0, 0, M_H^2, 0, M_W^2, M_W^2, M_W^2) \\
&\quad +2c_W^4(1-2s_W^2)\Big[D_{13} + D_{33}\Big](M_Z^2, s_{12}, M_H^2, s_{13}, 0, 0, 0, 0, M_W^2, M_W^2) \\
&\quad +2c_W^4\Big[2c_W^2\Big(D_{11} + D_{12}\Big) + \big(s_W^2 - c_W^2\big)D_2\Big](s_{13}, M_Z^2, s_{23}, 0, 0, M_H^2, 0, M_W^2, M_W^2, M_W^2)\Bigg\}. \qquad (14)
\end{aligned}
$$

It is stress that one has the following relation:

$$
F_{12}^{(G_3)}(s_{12}, s_{13}, s_{23}) = F_{13}^{(G_3)}(s_{13}, s_{12}, s_{23}). \qquad (15)
$$

If we apply several transformations for box-functions, we can confirm the relation. The transformations for box-functions are not presented in this subsection. Instead of this, we verify the relation by numerical check. One finds that two representations for $F_{13}^{(G_3)}$ in (14) and (15) are good agreement up to last digit at several sampling points.

Having all form factors, the decay rates can be evaluated as follows:

$$
\begin{aligned}
\Gamma_{H\to Z\nu_l\bar{\nu}_l} &= \frac{1}{256\pi^3 M_H^3 M_Z^2}\int_{4m_{\nu_l}^2}^{(M_H-M_Z)^2} ds_{23}\int_{s_{12}^{\min}}^{s_{12}^{\max}} ds_{12}\times \\
&\quad\times\Bigg\{\Big(M_Z^2(2s_{23}-M_H^2)+s_{12}s_{13}\Big)\Big[\Big|F_{00}^{(G_0)}\Big|^2 + 2\,\mathcal{R}\mathrm{e}\Big(F_{00}^{(G_0),*}\cdot\sum_{i=1}^{4}F_{00}^{(G_i)}\Big)\Big] \qquad (16) \\
&\quad +\Big(M_H^2M_Z^2 - s_{12}s_{13}\Big)\Big[\Big(M_Z^2 - s_{12}\Big)\mathcal{R}\mathrm{e}\Big(F_{00}^{(G_0),*}\cdot\sum_{i=1}^{4}F_{12}^{(G_i)}\Big) + \big(s_{12}\leftrightarrow s_{13}\big)\Big]\Bigg\}.
\end{aligned}
$$

Where

$$
s_{12}^{\max,\min} = \frac{1}{2}\Bigg\{M_H^2 + M_Z^2 - s_{23} \pm \sqrt{\Big(M_H^2 + M_Z^2 - s_{23}\Big)^2 - 4M_H^2M_Z^2}\Bigg\}. \qquad (17)
$$

The polarized Z boson case is next considered. The longitudinal polarization vectors for Z bosons are defined in the rest frame of Higgs boson:

$$
\varepsilon_\mu(q_1, \lambda = 0) = \frac{4M_{H^*}^2\; q_{1,\mu} - (s_{23} + M_Z^2)\; p_{H,\mu}}{M_Z\sqrt{\lambda(s_{23}, 4M_{H^*}^2, M_Z^2)}}. \qquad (18)
$$

Where off-shell Higgs mass is given by $p_H^2 = M_{H^*}^2 \neq M_H^2$. The Kallën function is defined as $\lambda(x,y,z) = (x-y-z)^2 - 4yz$. We then arrive at

$$\begin{aligned}\Gamma_{H\to Z_L\nu_l\bar{\nu}_l} &= \frac{1}{256\pi^3 M_{H^*}^3 M_Z^2}\int\limits_{4m_{\nu_l}^2}^{(M_{H^*}-M_Z)^2} ds_{23}\int\limits_{s_{12}^{\min}}^{s_{12}^{\max}} ds_{12}\frac{\Big(s_{23}-4M_{H^*}^2+M_Z^2\Big)\Big(s_{12}s_{13}-M_Z^2M_{H^*}^2\Big)}{[s_{23}-M_Z^2-4M_{H^*}^2]^2-16M_Z^2M_{H^*}^2}\times \\ &\times\Bigg\{\Big(s_{23}-4M_{H^*}^2+M_Z^2\Big)\Big[\Big|F_{00}^{(G_0)}\Big|^2+2\,\mathcal{R}\mathrm{e}\Big(F_{00}^{(G_0),*}\times\sum_{i=1}^{4}F_{00}^{(G_i)}\Big)\Big] \\ &+\Big[\Big(s_{23}^2-M_Z^4+4M_{H^*}^2M_Z^2\Big)+\Big(s_{23}-4M_{H^*}^2+M_Z^2\Big)s_{12}\Big]\times \\ &\times\mathcal{R}\mathrm{e}\Big(F_{00}^{(G_0),*}\sum_{i=1}^{4}F_{12}^{(G_i)}\Big)+\big(s_{12}\leftrightarrow s_{13}\big)\Bigg\}.\end{aligned} \tag{19}$$

Where $s_{12}^{\min,\,\max}$ are obtained as in equation (17) in which M_H is replaced by off-shell Higgs mass M_{H^*}.

In the next section, we show phenomenological results for the decay processes. Before generating the data, numerical checks for the calculations are performed. The UV- finiteness and μ^2-independent of the results are verified. Numerical results for this check are shown in Appendix B. One finds the results are good stability over 14 digits.

3. Phenomenological results

In the phenomenological results, we use the following input parameters: $M_Z = 91.1876$ GeV, $\Gamma_Z = 2.4952$ GeV, $M_W = 80.379$ GeV, $\Gamma_W = 2.085$ GeV, $M_H = 125.1$ GeV, $\Gamma_H = 4.07\cdot 10^{-3}$ GeV. The lepton masses are given: $m_e = 0.00052$ GeV, $m_\mu = 0.10566$ GeV and $m_\tau = 1.77686$ GeV. For quark masses, one takes $m_u = 0.00216$ GeV $m_d = 0.0048$ GeV, $m_c = 1.27$ GeV, $m_s = 0.93$ GeV, $m_t = 173.0$ GeV, and $m_b = 4.18$ GeV. We work in the so-called G_μ-scheme in which the Fermi constant is taken $G_\mu = 1.16638\cdot 10^{-5}$ GeV^{-2} and the electroweak coupling can be calculated appropriately as follows:

$$\alpha = \sqrt{2}/\pi G_\mu M_W^2(1-M_W^2/M_Z^2) = 1/132.184. \tag{20}$$

We then present the phenomenological results in the following subsections. We first mention about the decay rates for on-shell Higgs decay $H\to Z\nu_l\bar{\nu}_l$. In the Table 1, the decay rates for on-shell Higgs decay to $Z\nu_e\bar{\nu}_e$ are generated. In the first column, the cuts for invariant mass of final neutrino-pair are applied. The decay rates for the unpolarized case of the final Z boson are presented in the second column. The last column results are for the decay rates corresponding to the longitudinal polarization of the final Z boson. Furthermore, in this Table, we show for the tree level (and full one-loop) decay widths in the first (second) line, respectively. When we consider all generation of neutrinos, one should add to data by overall factor 3. The one-loop corrections are about $\sim 10\%$ contributions to the tree-level decay rates. We note that one-loop corrections are evaluated as follows:

$$\delta[\%] = \frac{\Gamma^{\rm Full}-\Gamma^{\rm Tree}}{\Gamma^{\rm Tree}}\times 100\%. \tag{21}$$

$m^{\rm cut}_{\nu_e\bar{\nu}_e}$ [GeV]	$\Gamma_{H\to Z\nu_e\bar{\nu}_e}$ [KeV]	$\Gamma_{H\to Z_L\nu_e\bar{\nu}_e}$ [KeV]
0	5.8177	2.2872
	6.4174	2.5061
5	5.7014	2.1736
	6.2902	2.3818
10	5.3401	1.8515
	5.8943	2.0293
20	3.7362	0.8389
	4.1305	0.9201

Table 1: The decay rates for on-shell Higgs decay into $Z\nu_e\bar{\nu}_e$. The first (second) line, we show for the tree level (and full one-loop) decay widths, respectively.

We next consider the off-shell Higgs decay to $Z\nu_e\bar{\nu}_e$. The numerical results are shown in the Table 2. In this case, we only consider the unpolarized of Z boson in the final state. In the first column, off-shell Higgs mass M_{H^*} is shown in the range of 200 GeV to 500 GeV. The off-shell decay widths are presented in the second column in which the first (second) line is for the tree-level (full one-loop) decay rates, respectively. It is worth to mention that the results in off-shell Higgs decays are good agreement with the decay rates in [16]. This means that the main contributions to the decay rates are from the values around the peak of Z-pole decay to $\nu_l\bar{\nu}_l$ (this explanation will be confirmed later).

M_{H^*} [GeV]	$\Gamma_{H\to Z\nu_e\bar{\nu}_e}$ [GeV]
200	0.0478
	0.0541
300	0.3383
	0.3789
400	1.0124
	1.1418
500	2.2101
	2.4865

Table 2: The decay rates for off-shell Higgs decay into $Z\nu_e\bar{\nu}_e$. The first (second) line, we show for the tree level (and full one-loop) decay widths, respectively.

For the experimental analyses, differential decay rates with respect to the invariant mass of neutrino-pair are of interests. These are corresponding to the decay rates of Higgs decay to Z plus missing energy. Thus, the data will provide the precise backgrounds for the signals of Higgs decay to lepton-pair when $Z \to$ lepton-pair is taken into account. This also contributes to the signals of $H \to$ invisible particles if the decay of final Z boson to neutrino-pair is considered. In Fig. 1, we show for the differential decay rates with respect to $m_{\nu_l\bar{\nu}_l}$ for the case of the unpolarized Z final state. We apply a cut of $m^{\rm cut}_{\nu_l\bar{\nu}_l} \geq 5$ GeV for this study. In the left panel, the triangle points are for the tree-level decay widths and the rectangle points are of full one-loop decay widths. In the right panel, the electroweak corrections are plotted. One finds that the corrections are range

of 9.4% to 10.8% contributions. In Fig. 2, the same distributions are shown in the longitudinal polarization of final Z boson. We use the same convention as previous case. We also find the corrections are range of 9.4% to 9.8% contributions.

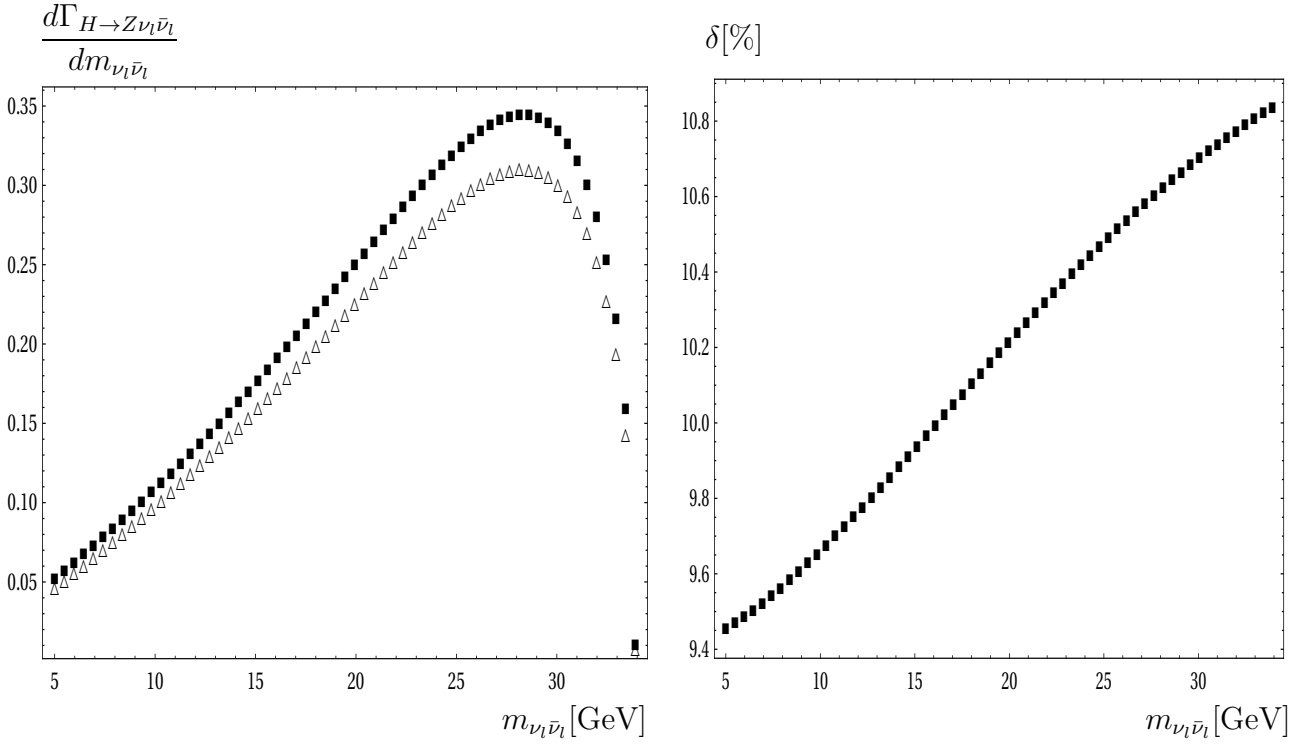


Figure 1: The differential decay rates (left panel) and corrections (right panel) with respect to $m_{\nu_l\bar{\nu}_l}$ for the unpolarized Z boson case. In the left panel, the triangle points show for the tree-level decay widths and the rectangle points present for full one-loop decay widths. In the right panel, the electroweak corrections are shown as the rectangle points.

The differential decay rates with respect to $m_{\nu_l\bar{\nu}_l}$ for off-shell Higgs case at $M_H^* = 500$ GeV are generated. In the Figs. 3, we observe a peak at $m_{\nu_l\bar{\nu}_l} = M_Z$ which is corresponding to $Z \to \nu_l\bar{\nu}_l$. The decay rates give large values around the peak and fall down rapidly beyond the peak. The corrections are from 10% to 25% in all range of $m_{\nu_l\bar{\nu}_l}$. We note that a cut of $m^{\rm cut}_{\nu_l\bar{\nu}_l} \geq 5$ GeV is employed in the distribution. From the distribution, it is shown that the main contributions to the off-shell Higgs decay rates come from the corresponding values around Z-peak. It explains that the off-shell Higgs decay rates in this work are good agreement with the results in [16]. This convinces the previous conclusion about the data in Table 2. For all range of Higgs mass, we also check numerically that the dominant contributions to the decay rates come from the Z-pole diagrams, or the diagrams of $H \to ZZ^* \to Z\nu_l\bar{\nu}_l$ (from group 1 and 2) in these decay channels. The same conclusion has pointed out in the paper [17].

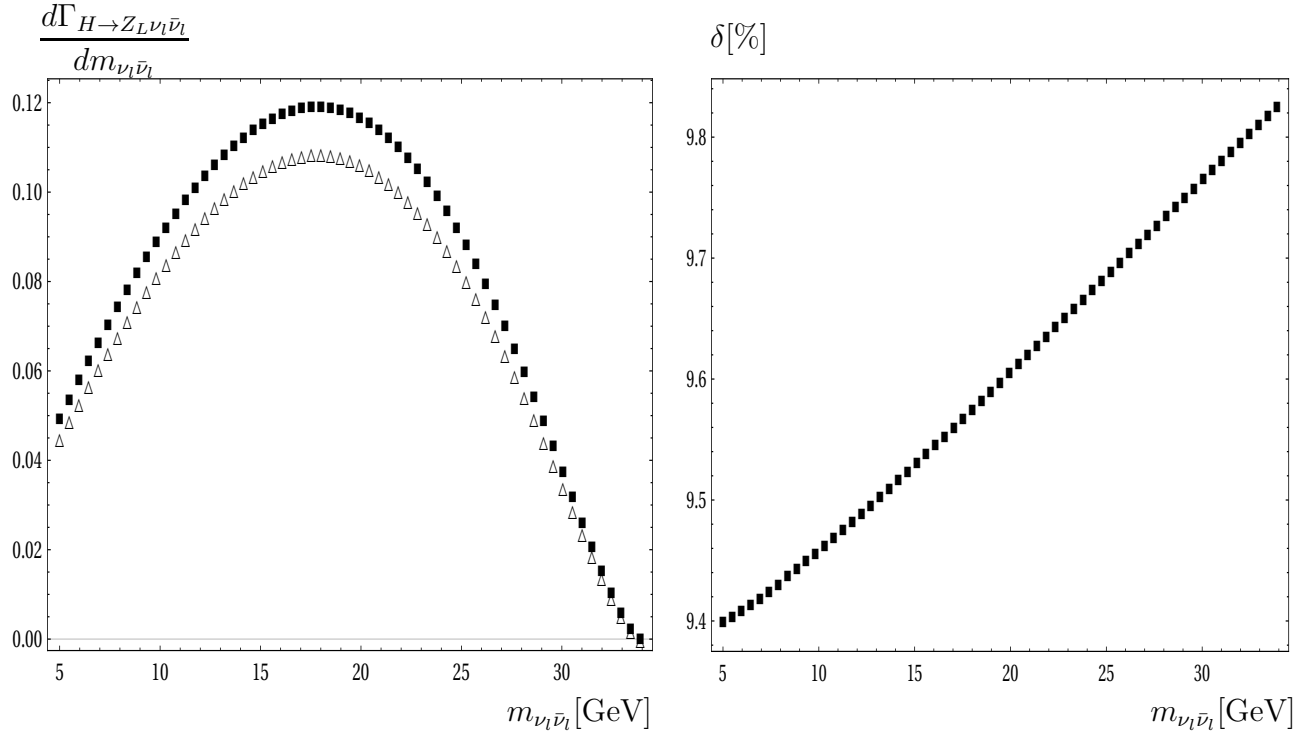


Figure 2: The differential decay rates (left panel) and corrections (right panel) with respect to $m_{\nu_l\bar{\nu}_l}$ in the longitudinal polarization case for Z boson. In the left Figure, the triangle points present for the tree-level decay widths and the rectangle points are for full one-loop decay widths. In the right Figure, the electroweak corrections are plotted as the rectangle points.

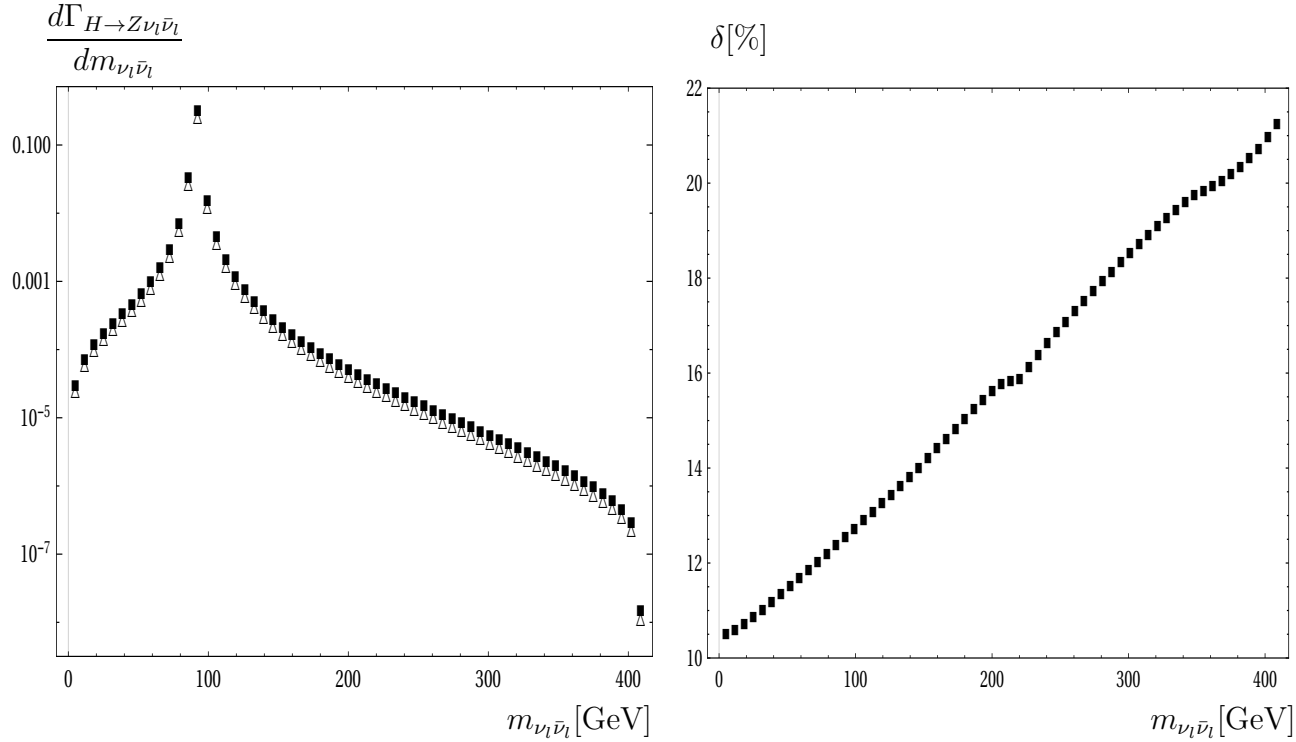


Figure 3: The differential decay rates (left panel) and corrections (right panel) with respect to $m_{\nu_l\bar{\nu}_l}$ for off-shell Higgs case. In the left panel, tree-level decay widths are plotted as triangle points and full one-loop decay widths are shown as rectangle points. In the right panel, the electroweak corrections are presented as the rectangle points.

We turn our attention to analyse the signals $H \to Z\nu_l\bar{\nu}_l$ through Higgs productiuon at future lepton collider such as $e^-e^+ \to ZH^* \to Z(Z\nu_l\bar{\nu}_l)$ with including the initial beam polarizations. Differential cross section with respect to M_{H^*} is given by [16]:

$$\frac{d\sigma^{e^-e^+\to ZH^*\to Z(Z\nu_l\bar{\nu}_l)}(\sqrt{s})}{dM_{H^*}} = (2M^2_{H^*}) \times \frac{\sigma^{e^-e^+\to ZH^*}(\sqrt{s}, M_{H^*})}{[(M^2_{H^*} - M^2_H)^2 + \Gamma^2_H M^2_H]} \times \frac{\Gamma_{H^*\to ZZ}(M_{H^*})}{\pi}. \quad (22)$$

Feynman diagram is depicted in the Fig. (4). We mention that cross section for $e^-e^+ \to ZH^*$

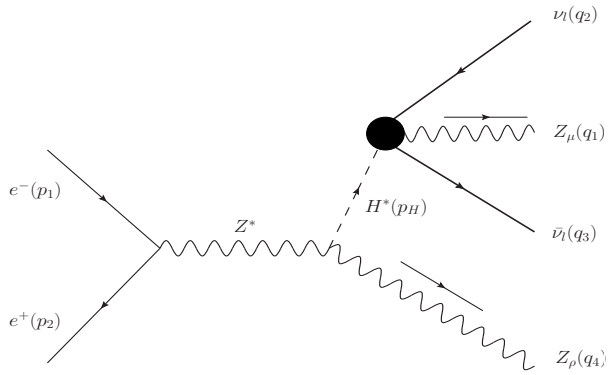


Figure 4: Feynman diagram for the processes $e^-e^+ \to Z(Z\nu_l\bar{\nu}_l)$ at the ILC with the blob representing for one-loop corrections to $H \to Z\nu_l\bar{\nu}_l$.

can be found in [16]. Total cross section for these processes can be computed as follows:

$$\sigma^{e^-e^+\to ZH^*\to Z(Z\nu_l\bar{\nu}_l)} = \int_{M_Z}^{\sqrt{s}-M_Z} dM_{H^*} \frac{d\sigma^{e^-e^+\to ZH^*\to Z(Z\nu_l\bar{\nu}_l)}(\sqrt{s})}{dM_{H^*}}. \quad (23)$$

In Table 3, we show cross sections for the signals of Higgs decay to $Z\nu_l\bar{\nu}_l$ via $e^-e^+ \to ZH^* \to Z(Z\nu_l\bar{\nu}_l)$ with including the initial beam polarizations (taking all three generations of neutrinos in the data). The second (third) column presents for the signals at tree level (full correction) cross sections respectively. The last column is for the SM backgrounds which are tree level of the reactions $e^-e^+ \to ZZ\nu_l\bar{\nu}_l$. The background processes are generated by using GRACE [19]. At each center-of-mass energy, the first line shows for LR case and second line is for RL polarization case. We show that the signals $H \to Z\nu_l\bar{\nu}_l$ can be probed at center-of-mass energy $\sqrt{s} = 250$ GeV and these are hard to measure at higher-energy regions due to the dominant of the backgrounds.

In the Fig. 5, we plot the distributions for cross section as functions of M_{H^*} at $\sqrt{s} = 500$ GeV of center-of-mass energy, considering the initial polarization cases for e^-e^+. Cross sections for LR case are shown in the left panel and for RL are presented in the right panel. For the signal cross sections, tree-level cross sections are plotted as dashed line and full one-loop cross sections are presented as solid line. While the SM backgrounds are shown as dotted points. The off-shell Higgs mass M_{H^*} is varied from M_Z to $\sqrt{s} - M_Z$. It is observed that the cross section are dominant around the on-shell Higgs mass $M_{H^*} \sim 125$ GeV. It is well-known that we have another peak which is around the ZH threshold ($\sim M_Z + M_H = 215$ GeV). Due to the small value of total decay width of Higgs boson, on-shell Higgs mass peak becomes more visible than the later one. In the off-shell Higgs mass region, cross sections are much smaller (about 2 order

$\sqrt{s}$ [GeV]	$\sigma_{\rm sig}^{\rm Tree}$ [fb]	$\sigma_{\rm sig}^{\rm Full}$ [fb]	$\sigma_{\rm bkg}$ [fb]
250	2.43873	2.69398	0.00309
	1.58487	1.74649	0.00016
500	0.68498	0.75668	16.7839
	0.44404	0.48932	1.33409
1000	0.26879	0.29692	164.146
	0.17424	0.19201	1.16635

Table 3: Total cross section of $e^-e^+ \to Z(Z\nu_l\bar{\nu}_l)$. First line results show for LR of e^-e^+, second line results present for RL of e^-e^+. Tree generations for neutrinos are taken into the results.

smaller) than the ones around the on-shell Higgs mass peak. We observe that the signals are clearly visible at on-shell Higgs mass $M_{H^*} = 125$ GeV. In the off-shell Higgs mass region, the SM backgrounds are much larger than the signals. These large contributions are mainly attributed to the dominant of t-channel diagrams appear in the background processes.

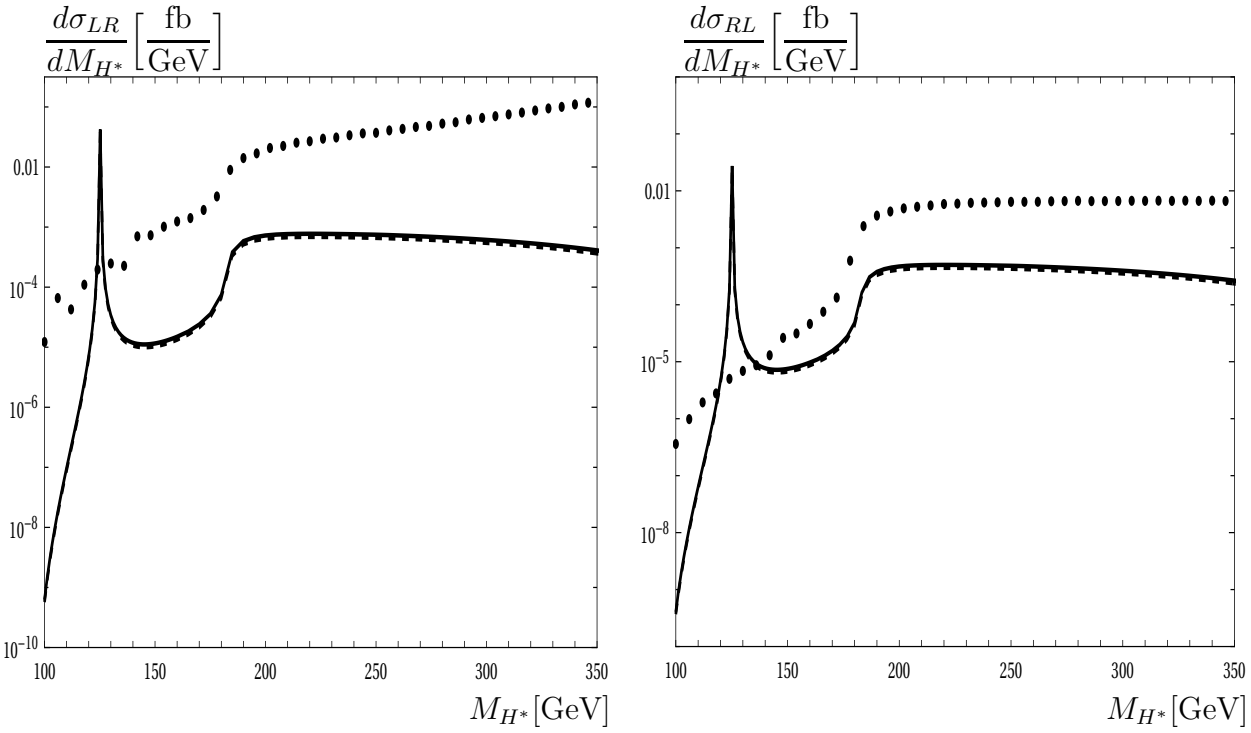


Figure 5: Off-shell Higgs decay rates as a function of M_{H^*} at center-of-mass energy $\sqrt{s} = 500$ GeV. Three generations for neutrinos are included in the results. Cross sections for LR case are shown in the left panel and for RL are presented in the right panel. For the signal cross sections, tree-level cross sections are shown as dashed line and full one-loop cross sections are shown as solid line. The dotted points are for the SM backgrounds.

Full one-loop electroweak corrections to the process $e^-e^+ \to ZH$ and the SM background processes with including the initial beam polarizations should be taken into account for the above analyses. The corrections can be generated by using the program [19], and recently study in [20]. Furthermore, by generalizing the couplings of Nambu-Goldstone bosons to Higgs, gauge bosons, etc as in [11], we can extend our work for many beyond the SM. These topics will be addressed in our future works.

4. Conclusions

Analytical results for one-loop contributing to the decay processes $H \to Z\nu_l\bar{\nu}_l$ for $l = e, \mu, \tau$ in 't Hooft-Veltman gauge have presented. The calculations have performed within the Standard Model framework. One-loop form factors are expressed in terms of the Passarino-Veltman functions in the standard conventions of `LoopTools` which the decay rates can be evaluated numerically. We have also studied the signals of $H \to Z\nu_l\bar{\nu}_l$ through Higgs productions at future lepton collider such as $e^-e^+ \to ZH^* \to Z(Z\nu_l\bar{\nu}_l)$ with including the initial beam polarizations. The SM background processes for this analysis have also taken into account. In phenomenological results, we find that one-loop corrections are about 10% contributions to the decay rates. They are sizeable contributions and should be included at future colliders. We show that the signals $H \to Z\nu_l\bar{\nu}_l$ are clearly visible at center-of-mass energy $\sqrt{s} = 250$ GeV and these are hard to probe at higher-energy regions due to the dominant of the background.

Acknowledgment: This research is funded by Vietnam National Foundation for Science and Technology Development (NAFOSTED) under the grant number 103.01-2019.346.

Appendix *A*: Tensor reduction

We show all tensor one-loop reduction formulas which have applied for this calculation in this appendix. The technique is based on the method in [13]. Tensor one-loop one-, two-, three- and four-point integrals with rank R are defined:

$$\{A; B; C; D\}^{\mu_1\mu_2\cdots\mu_R} = (\mu^2)^{2-d/2} \int \frac{d^dk}{(2\pi)^d} \frac{k^{\mu_1}k^{\mu_2}\cdots k^{\mu_R}}{\{P_1; P_1P_2; P_1P_2P_3; P_1P_2P_3P_4\}}. \tag{24}$$

Where the inverse Feynman propagators P_j $(j = 1, \cdots, 4)$ are given by

$$P_j = (k + q_j)^2 - m_j^2 + i\rho. \tag{25}$$

In this definition, the momenta $q_j = \sum_{i=1}^{j} p_i$ with p_i for the external momenta are taken into account and m_j for internal masses in the loops. The internal masses can be real and complex in the calculation. Following the dimensional regularization method, one-loop integrals are peformed in space-time dimension $d = 4 - 2\varepsilon$. The renormalization scale is introduced as μ^2 in this definition that help to track of the correct dimension of the integrals in space-time dimension d. If the numerators of one-loop integrands in Eq. (24) are 1, we have the corresponding scalar one-loop functions (noted as A_0, B_0, C_0 and D_0). All reduction formulas for one-loop tensor integrals up to rank $R = 3$ are are presented in the following paragraphs. In detail, one has the reduction expressions for one-loop two-point tensor integrals as

$$\begin{aligned}
A^\mu &= 0, && (26)\\
A^{\mu\nu} &= g^{\mu\nu}A_{00}, && (27)\\
A^{\mu\nu\rho} &= 0, && (28)\\
B^\mu &= q^\mu B_1, && (29)\\
B^{\mu\nu} &= g^{\mu\nu}B_{00} + q^\mu q^\nu B_{11}, && (30)\\
B^{\mu\nu\rho} &= \{g, q\}^{\mu\nu\rho}B_{001} + q^\mu q^\nu q^\rho B_{111}, && (31)
\end{aligned}$$

Reduction formulas for one-loop tensor three-point integrals are shown as

$$C^{\mu} = q_1^{\mu} C_1 + q_2^{\mu} C_2 = \sum_{i=1}^{2} q_i^{\mu} C_i, \tag{32}$$

$$C^{\mu\nu} = g^{\mu\nu} C_{00} + \sum_{i,j=1}^{2} q_i^{\mu} q_j^{\nu} C_{ij}, \tag{33}$$

$$C^{\mu\nu\rho} = \sum_{i=1}^{2} \{g, q_i\}^{\mu\nu\rho} C_{00i} + \sum_{i,j,k=1}^{2} q_i^{\mu} q_j^{\nu} q_k^{\rho} C_{ijk}, \tag{34}$$

For four-point functions, we have simillarly reduction expressions:

$$D^{\mu} = q_1^{\mu} D_1 + q_2^{\mu} D_2 + q_3^{\mu} D_3 = \sum_{i=1}^{3} q_i^{\mu} D_i, \tag{35}$$

$$D^{\mu\nu} = g^{\mu\nu} D_{00} + \sum_{i,j=1}^{3} q_i^{\mu} q_j^{\nu} D_{ij}, \tag{36}$$

$$D^{\mu\nu\rho} = \sum_{i=1}^{3} \{g, q_i\}^{\mu\nu\rho} D_{00i} + \sum_{i,j,k=1}^{3} q_i^{\mu} q_j^{\nu} q_k^{\rho} D_{ijk}. \tag{37}$$

We have already used the short notation [13] $\{g, q_i\}^{\mu\nu\rho}$ which is written explicitly as follows: $\{g, q_i\}^{\mu\nu\rho} = g^{\mu\nu} q_i^{\rho} + g^{\nu\rho} q_i^{\mu} + g^{\mu\rho} q_i^{\nu}$. It is noted that all scalar coefficients $A_{00}, B_1, \cdots, D_{333}$ in the right hand sides of the above reduction formulas are so-called Passarino-Veltman functions [13]. These functions have implemented into `LoopTools` [15] for numerical computations.

Appendix B: Numerical checks

After having all the neccessary one-loop form factors, we are going to check the computation numerically. We find that F_{00} contains the UV-divergent. By taking the one-loop counter term which are corresponding to the $F_{00}^{(G_4)}$. The analytic expressions for $F_{00}^{(G_4)}$ are given in (54) in which all renormalization constants are shown in the appendix D.

In the Table (4), checking for the UV-finiteness of the results at a random point in phase space are presented. By varying C_{UV} parameters the amplitudes are good stability over more than 14 digits.

(C_{UV}, μ^2)	$2\,\mathcal{R}\mathrm{e}\{M^*_{\text{Tree}} M_{\text{1-Loop}}\}$
$(0, 1)$	$-0.0015130298318390845 - 0.0015131160592122863\,i$
$(10^2, 10^5)$	$-0.0015130298318393881 - 0.0015131160592122863\,i$
$(10^4, 10^{10})$	$-0.0015130298318233315 - 0.0015131160592122863\,i$

Table 4: Checking for the UV-finiteness of the results at an random point in phase space. The amplitude $M_{\text{1-Loop}}$ is included all one-loop diagrams and counterterm diagrams.

Appendix C: Self energy

All Self energy are presented in terms of PV- functions in 't Hooft-Veltman gauge.

Self energy A-A

Self-energy photon-photon functions are casted into two fermion and contributions as follows:

$$\Pi^{AA}(q^2) = \Pi^{AA}_{T,b}(q^2) + \Pi^{AA}_{T,f}(q^2). \tag{38}$$

Each part is given:

$$\Pi^{AA}_{T,b}(q^2) = \frac{e^2}{(4\pi)^2}\Bigg\{\big(4M_W^2+3q^2\big)B_0(q^2,M_W^2,M_W^2) - 2(d-2)A_0(M_W^2)\Bigg\}, \tag{39}$$

$$\Pi^{AA}_{T,f}(q^2) = \frac{e^2}{(4\pi)^2}\Bigg\{-2\sum_f N_f^C Q_f^2\Big[4B_{00}(q^2,m_f^2,m_f^2) + q^2B_0(q^2,m_f^2,m_f^2) - 2A_0(m_f^2)\Big]\Bigg\}. \tag{40}$$

Self energy Z-A

Self-energy functions for Z-A mixing are written as the same previous form. Each part is presented accordingly

$$\Pi^{ZA}_{T,b}(q^2) = \frac{e^2}{(32\pi^2)(d-1)s_Wc_W}\Bigg\{2(d-2)\Big[c_W^2(2d-3)-s_W^2\Big]A_0(M_W^2) \tag{41}$$

$$-\Big\{4M_W^2\Big[c_W^2(3d-4)+(d-2)s_W^2\Big] + q^2\Big[c_W^2(6d-5)+s_W^2\Big]\Big\}B_0(q^2,M_W^2,M_W^2)\Bigg\},$$

$$\Pi^{ZA}_{T,f}(q^2) = \frac{e^2}{(32\pi^2)s_Wc_W}\Bigg\{2\sum_f N_f^C Q_f\Big(2s_W^2Q_f - T_f^3\Big)\times \tag{42}$$

$$\times\Big[4B_{00}(q^2,m_f^2,m_f^2) + q^2B_0(q^2,m_f^2,m_f^2) - 2A_0(m_f^2)\Big]\Bigg\}.$$

Self energy Z-Z

Self energy functions for Z-Z are shown in terms of scalar one-loop integrals as follows:

$$\begin{aligned}\Pi^{ZZ}_{T,b}(q^2) = \frac{e^2}{(64\pi^2)(d-1)q^2s_W^2c_W^4}\Bigg\{&2q^2c_W^2(2-d)\Big[c_W^4(4d-7)+s_W^2(s_W^2-2c_W^2)\Big]A_0(M_W^2)\\ &+c_W^2\Big[M_H^2-M_Z^2-(d-2)q^2\Big]A_0(M_H^2) + c_W^2\Big[M_Z^2-M_H^2-(d-2)q^2\Big]A_0(M_Z^2)\\ &+\Big\{2q^2\Big[c_W^2(M_H^2+M_Z^2)-2M_W^2(d-1)\Big] - c_W^2\Big[(M_H^2-M_Z^2)^2+q^4\Big]\Big\}B_0(q^2,M_H^2,M_Z^2)\\ &+\Big\{4M_W^2\Big[(3c_W^4-s_W^4)(2d-3)-2c_W^2s_W^2\Big]\\ &+q^2\Big[3c_W^4(4d-3)+(2c_W^2-s_W^2)s_W^2\Big]\Big\}c_W^2q^2B_0(q^2,M_W^2,M_W^2)\Bigg\},\end{aligned} \tag{43}$$

$$\Pi^{ZZ}_{T,f}(q^2) = \frac{e^2}{(16\pi^2)s_W^2c_W^2}\sum_f N_f^C\times \tag{44}$$

$$\times\Bigg\{\Big[(T_f^3)^2\big(2m_f^2-q^2\big)+2q^2Q_fs_W^2\big(T_f^3-Q_fs_W^2\big)\Big]B_0(q^2,m_f^2,m_f^2)$$

$$+\Big[4Q_fs_W^2(T_f^3-Q_fs_W^2)-2(T_f^3)^2\Big]\Big[2B_{00}(q^2,m_f^2,m_f^2)-A_0(m_f^2)\Big]\Bigg\}.$$

Self energy W-W

Self-energy functions for W-W are presented correspondingly

$$\begin{aligned}
\Pi_{T,b}^{WW}(q^2) &= \frac{e^2}{(64\pi^2)(d-1)q^2 s_W^2 c_W^2}\Bigg\{ c_W^2\Big[M_H^2 - M_W^2 - (d-2)q^2\Big]A_0(M_H^2) \\
&+c_W^2\Big[2M_W^2 - M_H^2 - M_Z^2 - 2q^2(2d-3)(d-2)\Big]A_0(M_W^2) \\
&+c_W^2\Big[4c_W^2(d-2)+1\Big]\Big[M_Z^2 - M_W^2 - (d-2)q^2\Big]A_0(M_Z^2) \\
&+\Big\{c_W^2 q^4\Big[4c_W^2(3d-2)-1\Big] - c_W^2(M_W^2 - M_Z^2)^2\Big[4c_W^2(d-2)+1\Big] \\
&+2q^2 M_W^2\Big[2c_W^4(3d-5) - 2s_W^4(d-1) + 3c_W^2(2d-3)+1\Big]\Big\}B_0(q^2, M_W^2, M_Z^2) \\
&+c_W^2\Big\{2q^2\Big[(3-2d)M_W^2 + M_H^2\Big] - (M_H^2 - M_W^2)^2 - q^4\Big\}B_0(q^2, M_H^2, M_W^2) \\
&+4c_W^2 s_W^2\Big\{M_W^2(2q^2 - M_W^2)(d-2) + (3d-2)q^4\Big\}B_0(q^2, 0, M_W^2)\Bigg\},
\end{aligned} \tag{45}$$

$$\begin{aligned}
\Pi_{T,f}^{WW}(q^2) &= \frac{e^2}{(64\pi^2)s_W^2 c_W^2}\Bigg\{2c_W^2\sum_{\text{doublet}} N_f^C\Big[\Big(m_f^2 + m_{f'}^2 - q^2\Big)B_0(q^2, m_{f'}^2, m_f^2) \\
&\qquad -4B_{00}(q^2, m_{f'}^2, m_f^2) + A_0(m_f^2) + A_0(m_{f'}^2)\Big]\Bigg\}.
\end{aligned} \tag{46}$$

Self energy H-H

The expressions for self-energy H-H are written

$$\begin{aligned}
\Pi_b^{HH}(q^2) &= \frac{e^2}{(128\pi^2)M_W^2 s_W^2 c_W^4}\Bigg\{3M_H^2 c_W^4\Big[3M_H^2 B_0(q^2, M_H^2, M_H^2) + A_0(M_H^2)\Big] \\
&+2c_W^4\Big\{4M_W^2\Big[M_W^2(d-1) - q^2\Big] + M_H^4\Big\}B_0(q^2, M_W^2, M_W^2) \\
&+\Big\{c_W^4 M_H^4 + 4M_W^2\Big[M_W^2(d-1) - c_W^2 q^2\Big]\Big\}B_0(q^2, M_Z^2, M_Z^2) \\
&+2c_W^4\Big[2M_W^2(d-1) + M_H^2\Big]A_0(M_W^2) + \Big[c_W^4 M_H^2 + 2M_W^2 c_W^2(d-1)\Big]A_0(M_Z^2)\Bigg\},
\end{aligned} \tag{47}$$

$$\begin{aligned}
\Pi_f^{HH}(q^2) &= \frac{e^2}{(128\pi^2)M_W^2 s_W^2 c_W^4} \times \\
&\times\Bigg\{4c_W^4\sum_f N_f^C m_f^2\Big[(q^2 - 4m_f^2)B_0(q^2, m_f^2, m_f^2) - 2A_0(m_f^2)\Big]\Bigg\} - \frac{3\delta T}{v}.
\end{aligned} \tag{48}$$

Where $v = 246$ GeV is vacuum expectation value.

The tadpole

The tadpole is calculated as follows:

$$T_b^{loop} = \frac{e}{(64\pi^2)M_W s_W c_W^2}\Bigg\{\Big[c_W^2 M_H^2 + 2M_W^2(d-1)\Big]A_0(M_Z^2) \\ +2c_W^2\Big[2M_W^2(d-1)+M_H^2\Big]A_0(M_W^2) + 3M_H^2 c_W^2 A_0(M_H^2)\Bigg\}, \tag{49}$$

$$T_f^{loop} = -\frac{8e\, c_W^2}{(64\pi^2)M_W s_W c_W^2}\sum_f N_f^C m_f^2 A_0(m_f^2). \tag{50}$$

We then have

$$\delta T = -(T_b^{loop} + T_f^{loop}). \tag{51}$$

In case of neutrino, explicit expressions for self-energy functions ν_l-ν_l as follows

$$\Sigma^{\nu_l}(q^2) = \mathcal{K}_\gamma^{\nu_l}(q^2)\not{q} + \mathcal{K}_{5\gamma}^{\nu_l}(q^2)\not{q}\gamma_5 \tag{52}$$

where

$$\mathcal{K}_\gamma^{\nu_l}(q^2) = -\mathcal{K}_{5\gamma}^{\nu_l}(q^2) = -\frac{e^2}{128\pi^2 s_W^2 c_W^2}\Bigg[(2c_W^2+1) + 2B_1(q^2,0,M_Z^2) \\ +2c_W^2\sum_l\Big(\frac{m_l^2}{M_W^2}+2\Big)B_1(q^2,m_l^2,M_W^2)\Bigg]. \tag{53}$$

Appendix *D*: Counterterms

The counterterms of the decay process $H \to Z\nu_l\bar{\nu}_l$ are written by

$$F_{00}^{(G_4)} = F_{00,Z\nu_l\bar{\nu}_l}^{(G_4)} + F_{00,HZZ}^{(G_4)} + F_{00,Z\chi_3}^{(G_4)} + F_{00,ZZ}^{(G_4)}, \tag{54}$$

where

$$F_{00,Z\nu_l\bar{\nu}_l}^{(G_4)} = \frac{2\pi\alpha M_W}{s_W^2 c_W^3}\frac{1}{s-M_Z^2+i\Gamma_Z M_Z}\Big(\delta Y + \delta G_2 + \delta G_3 + \delta Z_{ZZ}^{1/2} + 2\delta Z_{\nu_l L}^{1/2}\Big), \tag{55}$$

$$F_{00,HZZ}^{(G_4)} = \frac{2\pi\alpha M_W}{s_W^2 c_W^3}\frac{1}{s-M_Z^2+i\Gamma_Z M_Z}\Big(\delta Y + \delta G_2 + \delta G_3 + \delta G_Z + 2\delta Z_{ZZ}^{1/2} + \delta Z_H^{1/2}\Big), \tag{56}$$

$$F_{00,ZZ}^{(G_4)} = \frac{2\pi\alpha M_W}{s_W^2 c_W^3}\frac{1}{(s-M_Z^2+i\Gamma_Z M_Z)^2}\Big(2M_Z^2\,\delta G_Z + (M_Z^2-s)\delta Z_{ZZ}^{1/2}\Big). \tag{57}$$

While the contribution of $F_{00,Z\chi_3}^{(G_4)}$ is vanished due to Dirac equation.

All renormalization constants are given as

$$\delta Y = -\delta Z_{AA}^{1/2} + \frac{s_W}{c_W}\delta Z_{ZA}^{1/2}, \tag{58}$$

$$\delta G_2 = \delta G_Z - \delta H, \quad \delta G_3 = \delta G_Z - \delta G_W, \tag{59}$$

$$\delta H = \frac{\delta M_Z^2 - \delta M_W^2}{2(M_Z^2 - M_W^2)}, \quad \delta G_Z = \frac{\delta M_Z^2}{2M_Z^2}, \quad \delta G_W = \frac{\delta M_W^2}{2M_W^2}. \tag{60}$$

Other renormalization constants are read as

$$\delta Z_{AA}^{1/2} = \frac{1}{2}\frac{d}{dq^2}\Pi_T^{AA}(0) = \frac{1}{2}\frac{d}{dq^2}\Pi_T^{AA}(q^2)\Big|_{q^2=0}, \tag{61}$$

$$\delta Z_{ZA}^{1/2} = -\Pi_T^{ZA}(0)/M_Z^2 = -\Pi_T^{ZA}(q^2)/M_Z^2\Big|_{q^2=0}, \tag{62}$$

$$\delta M_W^2 = -\mathcal{R}\mathrm{e}\left\{\Pi_T^{WW}(M_W^2)\right\} = -\mathcal{R}\mathrm{e}\left\{\Pi_T^{WW}(q^2)\Big|_{q^2=M_W^2}\right\}, \tag{63}$$

$$\delta M_Z^2 = -\mathcal{R}\mathrm{e}\left\{\Pi_T^{ZZ}(M_Z^2)\right\} = -\mathcal{R}\mathrm{e}\left\{\Pi_T^{ZZ}(q^2)\Big|_{q^2=M_Z^2}\right\}, \tag{64}$$

$$\delta Z_{ZZ}^{1/2} = \frac{1}{2}\mathcal{R}\mathrm{e}\left\{\frac{d}{dq^2}\Pi_T^{ZZ}(q^2)\Big|_{q^2=M_Z^2}\right\} = \frac{1}{2}\mathcal{R}\mathrm{e}\left\{\Pi_T^{ZZ'}(q^2)\Big|_{q^2=M_Z^2}\right\}, \tag{65}$$

$$\delta Z_H^{1/2} = -\frac{1}{2}\mathcal{R}\mathrm{e}\left\{\frac{d}{dq^2}\Pi^{HH}(q^2)\Big|_{q^2=M_H^2}\right\} = -\frac{1}{2}\mathcal{R}\mathrm{e}\left\{\frac{d}{dq^2}\Pi^{HH}(q^2)\Big|_{q^2=M_H^2}\right\}, \tag{66}$$

$$\delta Z_{\nu_l L}^{1/2} = \frac{1}{2}\mathcal{R}\mathrm{e}\left\{\mathcal{K}_{5\gamma}^{\nu_l}(m_{\nu_l}^2) - \mathcal{K}_{\gamma}^{\nu_l}(m_{\nu_l}^2)\right\}. \tag{67}$$

Appendix *E*: Feynman diagrams

All Feynman diagrams contributing to the decay processes $H \to Z\nu_l\bar{\nu}_l$ in 't Hooft-Veltman are shown in this appendix.

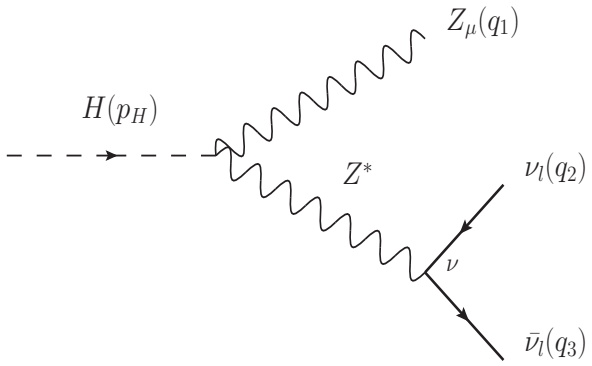


Figure 6: Group G_0: Tree level Feynman diagram.

References

[1] G. Aad *et al.* [ATLAS], Phys. Lett. B **716** (2012), 1-29 doi:10.1016/j.physletb.2012.08.020 [arXiv:1207.7214 [hep-ex]].

[2] S. Chatrchyan *et al.* [CMS], Phys. Lett. B **716** (2012), 30-61 doi:10.1016/j.physletb.2012.08.021 [arXiv:1207.7235 [hep-ex]].

[3] A. Liss *et al.* [ATLAS], [arXiv:1307.7292 [hep-ex]].

[4] [CMS], [arXiv:1307.7135 [hep-ex]].

[5] H. Baer, T. Barklow, K. Fujii, Y. Gao, A. Hoang, S. Kanemura, J. List, H. E. Logan, A. Nomerotski and M. Perelstein, *et al.* [arXiv:1306.6352 [hep-ph]].

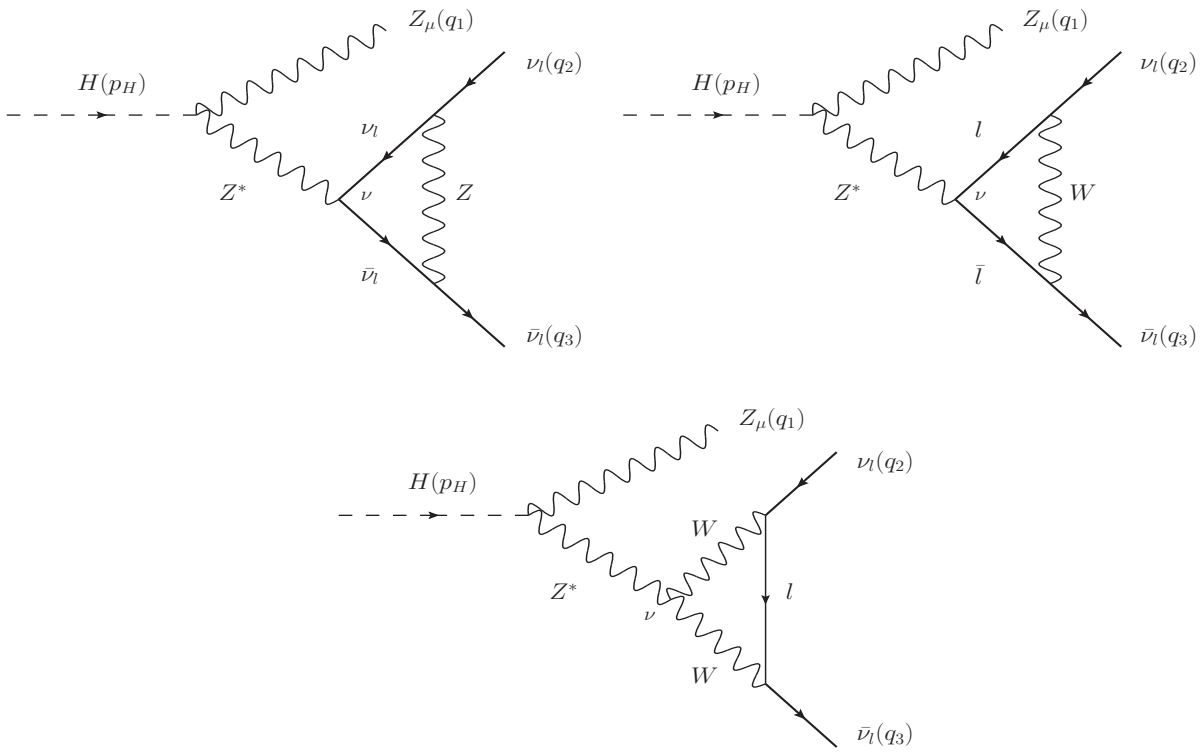


Figure 7: Group G_1: All one-loop Feynman diagrams contributing to the vertex $H\nu_l\bar{\nu}_l$.

[6] G. Aad *et al.* [ATLAS], JHEP **08** (2022), 104 doi:10.1007/JHEP08(2022)104 [arXiv:2202.07953 [hep-ex]].

[7] Z. Q. Chen, Q. M. Feng and C. F. Qiao, [arXiv:2107.04858 [hep-ph]].

[8] B. A. Kniehl and O. L. Veretin, Phys. Rev. D **86** (2012), 053007 doi:10.1103/PhysRevD.86.053007 [arXiv:1206.7110 [hep-ph]].

[9] A. Bredenstein, A. Denner, S. Dittmaier and M. M. Weber, Phys. Rev. D **74** (2006), 013004 doi:10.1103/PhysRevD.74.013004 [arXiv:hep-ph/0604011 [hep-ph]].

[10] A. Bredenstein, A. Denner, S. Dittmaier and M. M. Weber, JHEP **02** (2007), 080 doi:10.1088/1126-6708/2007/02/080 [arXiv:hep-ph/0611234 [hep-ph]].

[11] K. H. Phan, L. Hue and D. T. Tran, PTEP **2021** (2021) no.9, 093B05 doi:10.1093/ptep/ptab106 [arXiv:2103.14248 [hep-ph]].

[12] H. H. Patel, Comput. Phys. Commun. **197** (2015), 276-290

[13] A. Denner and S. Dittmaier, Nucl. Phys. B **734** (2006), 62-115

[14] A. Denner, Fortsch. Phys. **41** (1993), 307-420 doi:10.1002/prop.2190410402 [arXiv:0709.1075 [hep-ph]].

[15] T. Hahn and M. Perez-Victoria, Comput. Phys. Commun. **118** (1999), 153-165.

[16] K. H. Phan and D. T. Tran, [arXiv:2209.12410 [hep-ph]].

[17] A. Kachanovich, U. Nierste and I. Nišandžić, Phys. Rev. D **105** (2022) no.1, 013007 doi:10.1103/PhysRevD.105.013007 [arXiv:2109.04426 [hep-ph]].

[18] G. Belanger, F. Boudjema, J. Fujimoto, T. Ishikawa, T. Kaneko, K. Kato and Y. Shimizu, Phys. Rept. **430** (2006), 117-209 doi:10.1016/j.physrep.2006.02.001 [arXiv:hep-ph/0308080 [hep-ph]].

[19] G. Belanger, F. Boudjema, J. Fujimoto, T. Ishikawa, T. Kaneko, K. Kato and Y. Shimizu, Phys. Rept. **430** (2006), 117-209 doi:10.1016/j.physrep.2006.02.001 [arXiv:hep-ph/0308080 [hep-ph]].

[20] N. M. U. Quach, J. Fujimoto and Y. Kurihara, PTEP **2022** (2022) no.7, 073C01 doi:10.1093/ptep/ptac090 [arXiv:2204.08473 [hep-ph]].

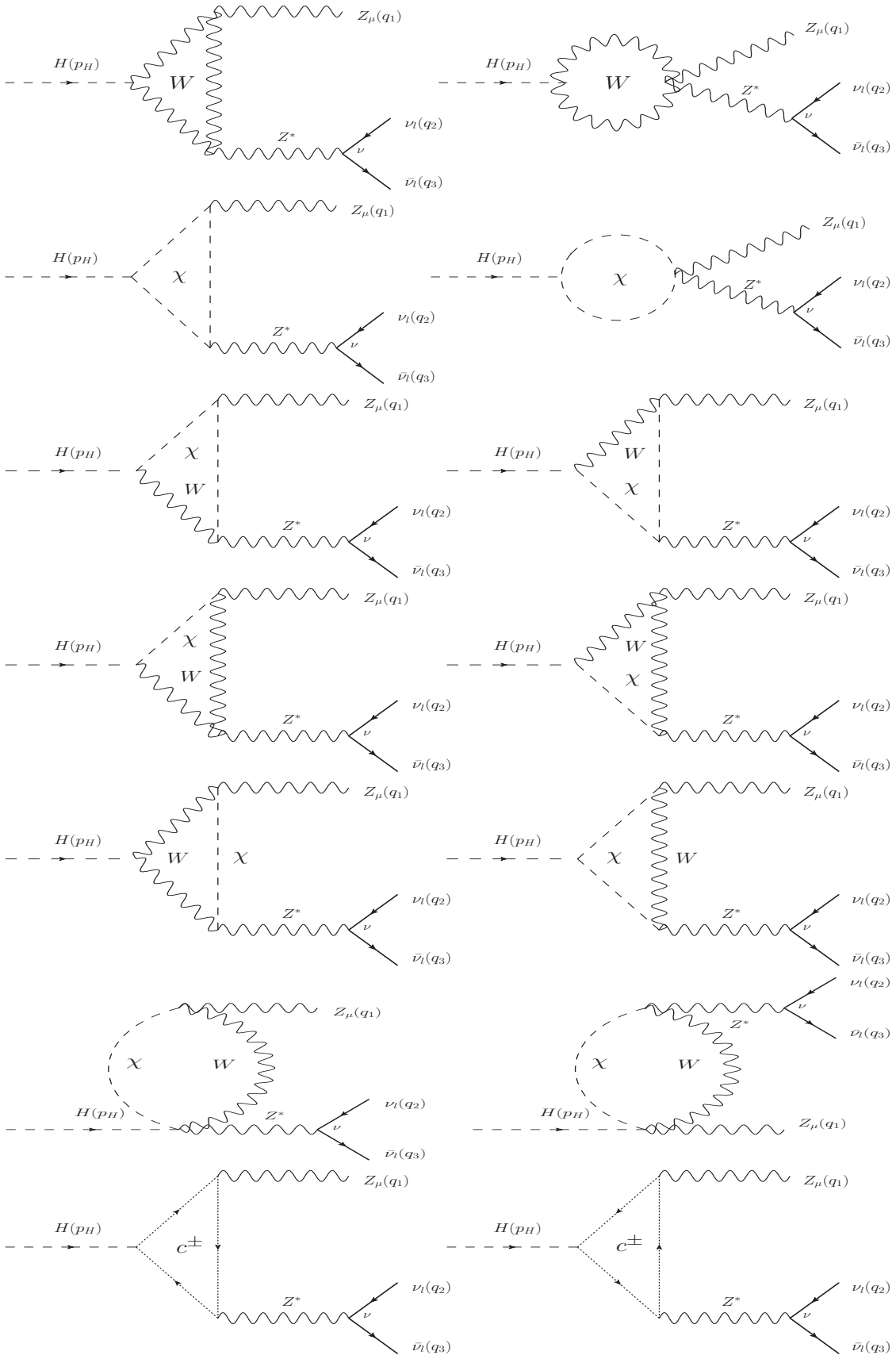


Figure 8: Group G_2: All Z-pole Feynman diagrams contributing to the decay process. We note that $\chi^\pm$ and $c^\pm$ are Nambu-Goldstone bosons and ghost particles, respectively.

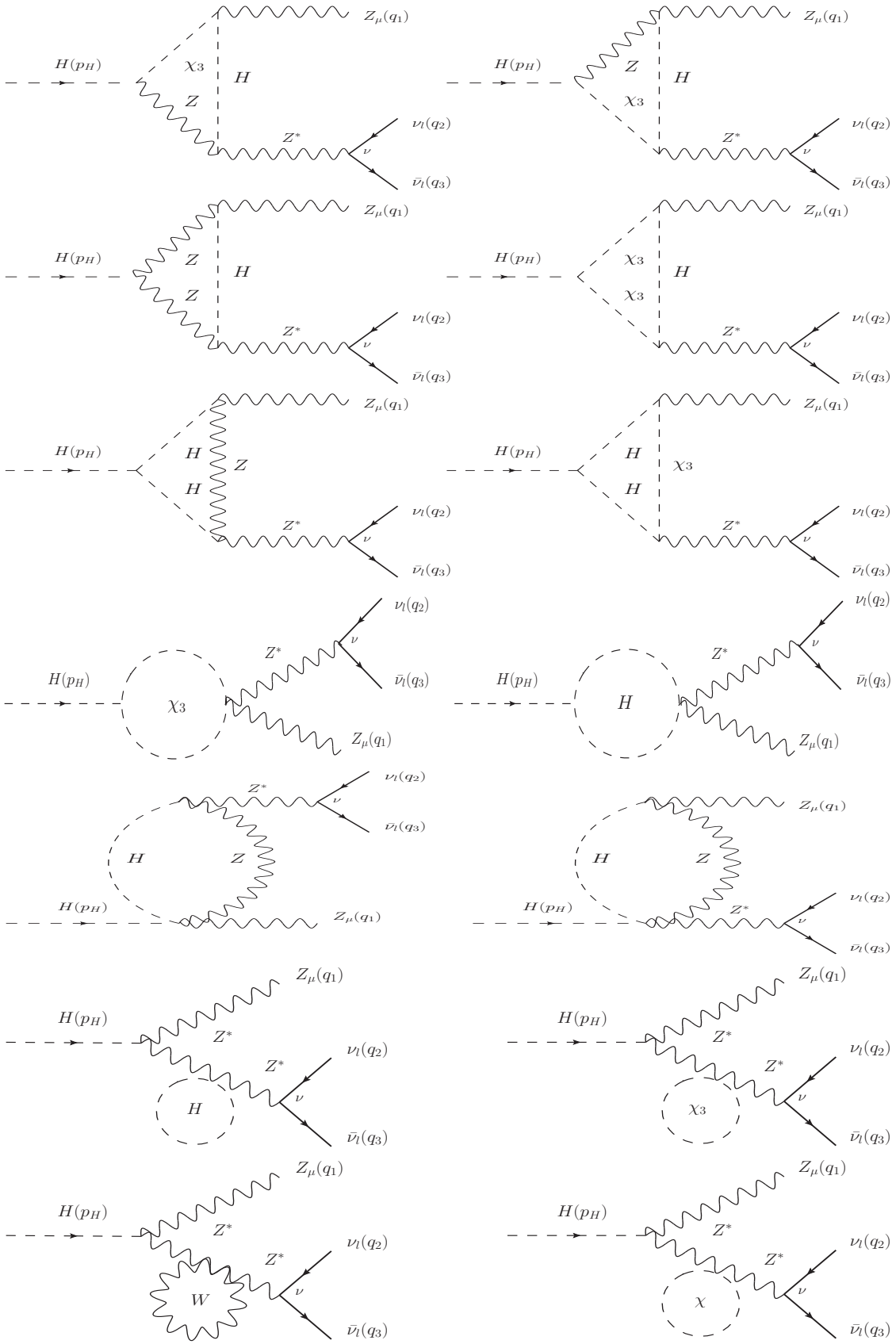


Figure 9: Group G_2: All Z-pole Feynman diagrams contributing to the decay process. We note that χ_3 is Nambu-Goldstone boson.

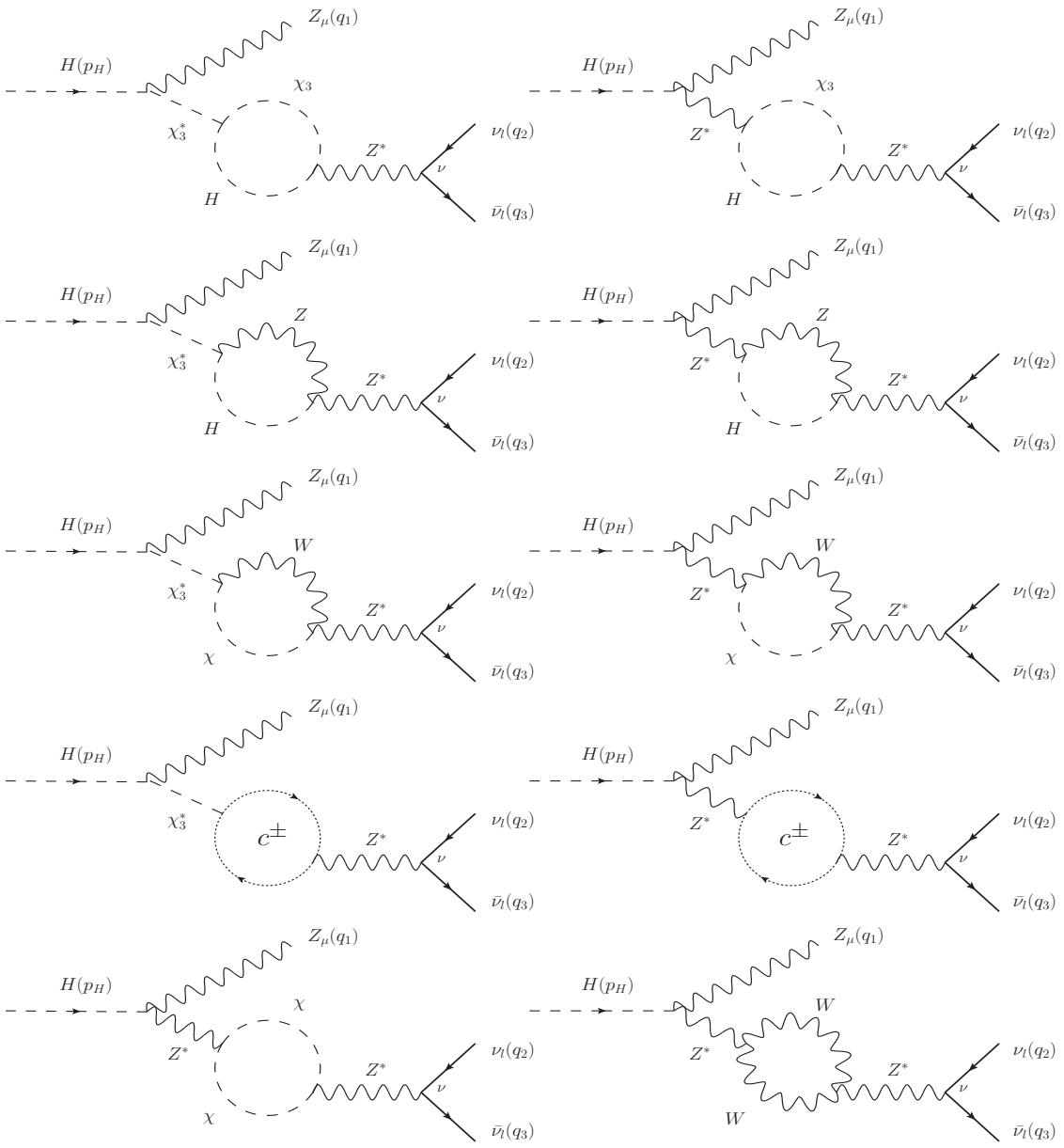


Figure 10: Group G_2: All Z-pole Feynman diagrams contributing to the decay process. We note that $\chi^\pm$ and $c^\pm$ are Nambu-Goldstone bosons and ghost particles, respectively.

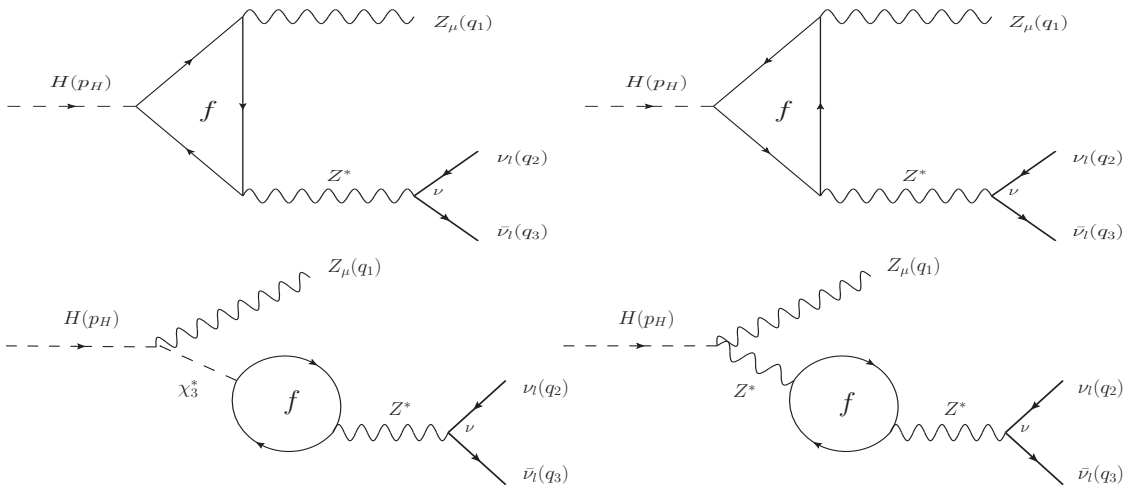


Figure 11: Group G_2: All Z-pole Feynman diagrams contributing to the decay process. Here, χ_3 is Nambu-Goldstone boson.

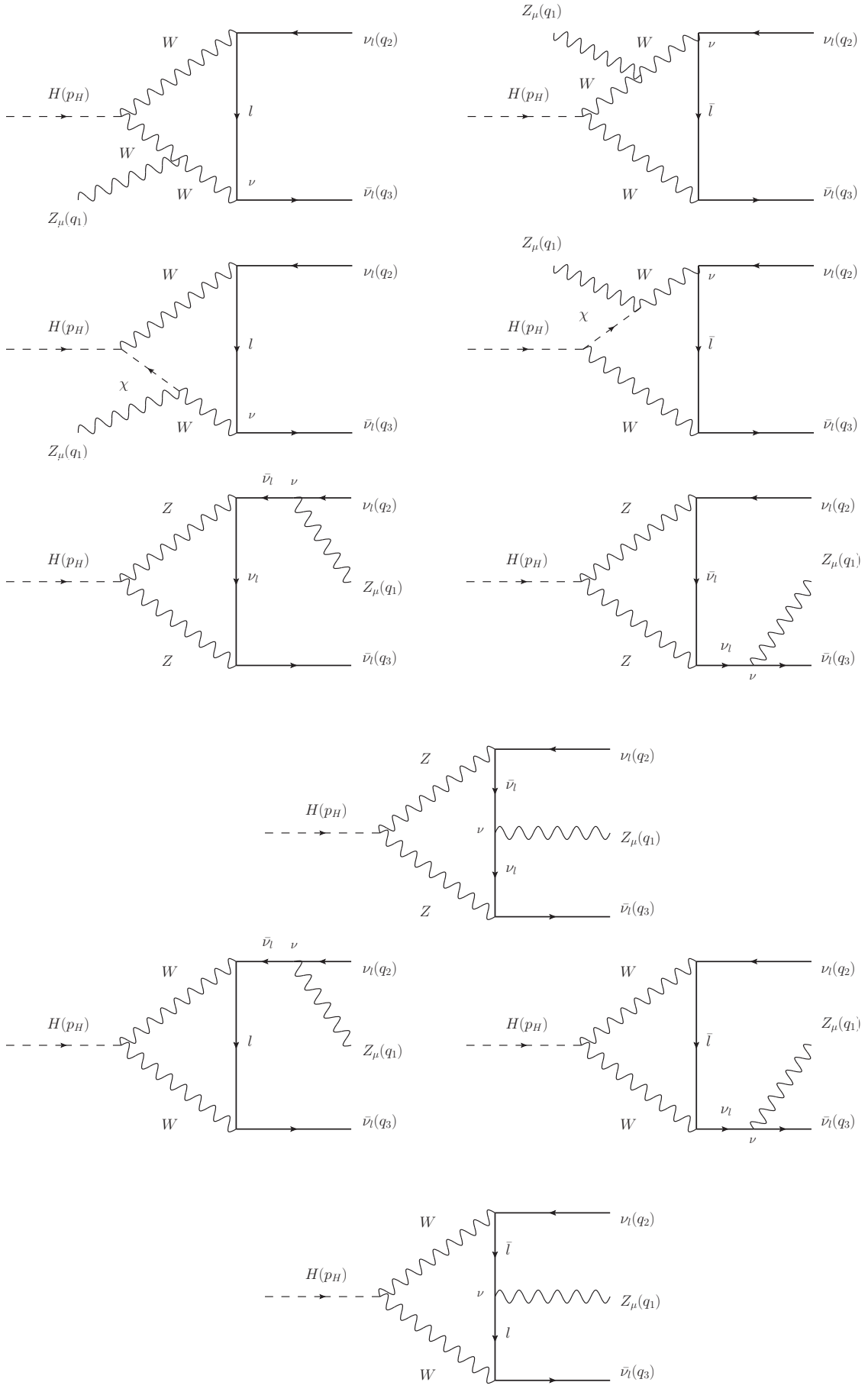


Figure 12: Group G_3: All non Z-pole Feynman diagrams contributing to the decay process. Here $\chi^\pm$ are Nambu-Goldstone bosons.

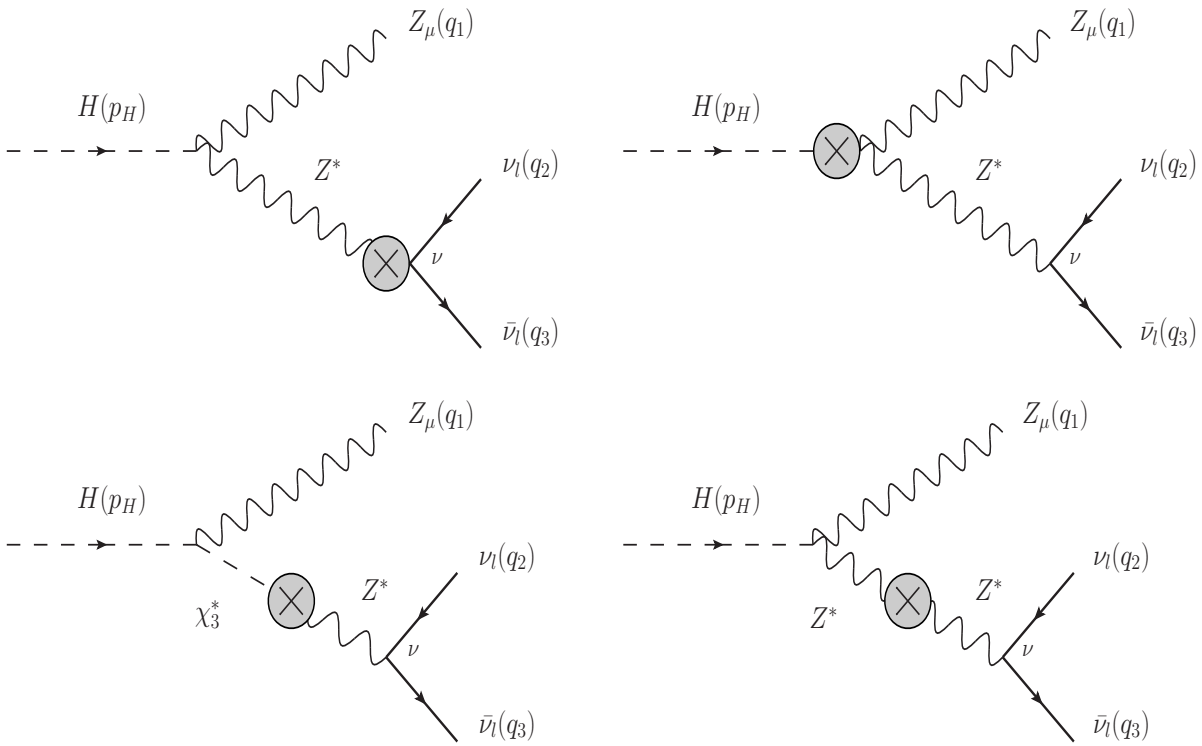


Figure 13: Group G_4: All counterterm Feynman diagrams contributing to the decay process.